ACS Macro Letters
Letter
pubs.acs.org/macroletters

Highly Aligned Block Copolymer Thin Films by Synergistic Coupling of Static Graphoepitaxy and Dynamic Thermal Annealing Fields

Brian C. Berry,*[†] Gurpreet Singh,[‡] Ho-Cheol Kim,[§] and Alamgir Karim*[‡]

[†]Department of Chemistry, University of Arkansas at Little Rock, Little Rock, Arkansas 72204, United States
[‡]Department of Polymer Engineering, The University of Akron (UA), Akron, Ohio 44325, United States
[§]IBM Research Division, Almaden Research Center, San Jose, California 95120-6099, United States

Ⓢ *Supporting Information*

ABSTRACT: Directed self-assembly of cylinder forming block copolymer (c-BCP) thin films via a dynamic thermal field on multidimensional symmetric graphoepitaxy channels is reported. A synergy of dynamic thermal and static boundary fields induces highly aligned c-BCP cylinders inside the channels with a power law dependence of orientational order parameter *f*, on trench width, $f \sim d^{-0.3}$, analogous to dual-field alignment of semiconducting metals and liquid crystals on graphoepitaxy surfaces, $f' \sim d^{-1}$. Static thermal annealing of identical films in a vacuum oven for several days fails to produce comparable results. Furthermore, we demonstrate global c-BCP cylinder alignment over mesas and trenches by tuning the synergy between the dynamic thermal field and asymmetry of the graphoepitaxy static field.

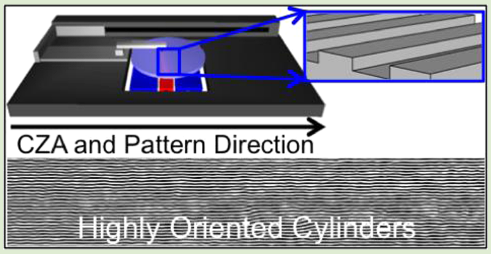

The search for alternate routes toward smaller nanostructures to supplement the conventional photolithographic process, which continues to encounter mounting challenges, has turned the attention of industry and researchers alike toward self-assembled block copolymer (BCP) thin films. BCPs can self-assemble to form nanostructures as small as 5 nm;[1−6] however, in the absence of an external driving force, these nanostructures lack the long-range order necessary for most applications. Several researchers have demonstrated that it is indeed possible to precisely guide the self-assembly of BCPs via various methods, such as electric fields,[7] temperature gradients,[8−12] shear fields,[11,13−15] faceted substrates,[16,17] etc.,[18−22] to create large arrays of highly ordered nanostructures. Of these, graphoepitaxy[23−25] and chemoepitaxial[26−29] field based directed self-assembly (DSA) methods have enjoyed the most success in recent times.

Previously, fabricating graphoepitaxy surfaces was a tedious and rate-limiting process involving complex processes such as e-beam writing or photolithography, but presently[30] step and flash imprint lithography[31] or nanoimprint lithography[32] have proven to be faster, easier, and robust routes toward large-scale fabrication of graphoepitaxy surfaces, thus making graphoepitaxy a highly attractive large-scale BCP DSA method. The fundamental challenge concerning BCP graphoepitaxy however is the rate at which BCP self-assembles into highly ordered arrays of nanostructures.[33,34] Current research data[23,30,35,36] indicate that BCP thin film graphoepitaxy leads to highly ordered structures only when supplemented with thermal annealing in a vacuum oven for extremely long time periods ≈ 12−72 h and at very high temperatures ≈ 200−250 °C. Use of solvents to impart higher mobility to the BCP phases in conjunction with graphoepitaxy and/or heat definitely facilitates rapid BCP self-assembly as has been recently demonstrated.[33,37] However, the use of solvents on an industrial scale would require significant new infrastructure for the semiconductor processing industry. Most solvents that facilitate BCP DSA are volatile, toxic in nature, and can pose significant health and environmental risks. Additionally, organic solvents are not compatible with most flexible substrates that might be needed for future flexible devices. However, it is true that if solvent-based methods are proven to be indispensible then the industry will not hesitate at scaling up these methods irrespective of the potential high cost. With these challenges in mind, recently there has been renewed interest in dynamic thermal fields or zone annealing (ZA) as the BCP DSA method of choice.[8,9,12] The ZA method adopted from metallurgy[38] involves passing the BCP thin film through a temperature gradient so as to controllably restrict the grain growth in a narrow region followed by its propagation throughout the film. The ZA process is performed at temperatures much lower than the BCP order−disorder transition temperature, and thus the process is referred to as cold zone annealing or “CZA”. BCP-CZA has proven to be extremely useful to direct BCP self-assembly for continuous fabrication of highly ordered nanostructures over unlimited dimensions, with faster ordering kinetics and orientation control as compared to the conventional thermal vacuum oven annealing. Furthermore, CZA is highly compatible to semiconductor processing. We recently demonstrated a novel CZA method, termed as CZA-SS, to couple a dynamic shear field to a dynamic thermal field for

Received: February 5, 2013
Accepted: March 29, 2013
Published: April 8, 2013

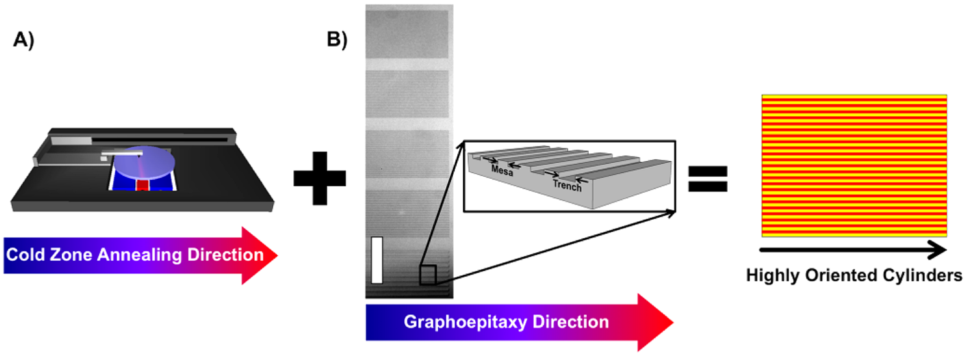

Figure 1. Schematic of the cold zone annealing process over the multidimensional graphoepitaxy channels. (A) Schematic of the cold zone annealing platform. (B) Optical micrograph showing the topographical features used in this experiment. The patterned areas are constant pitch with line sizes ranging from 400 nm (top) to 2 μm (bottom). The scale bar represents 40 μm. The arrow indicates the direction of annealing for these experiments.

rapid fabrication (12 mm/min) of highly oriented hierarchical nanostructures on rigid and flexible substrates.[11] Furthermore, CZA-SS can orient the BCP nanostructures independently of the imprint mold pattern direction, which is extremely difficult with conventional mold patterning methods.

Here, we demonstrate the ability to exploit the synergy between the aligning forces of the static graphoepitaxy field with the dynamic CZA field to fabricate highly oriented horizontal BCP cylinders at a fraction of the time required to orient the film if they were to be conventionally annealed in a vacuum oven. Our focus here is on studying the DSA-CZA of cylindrical BCP thin films on graphoepitaxy surfaces as a function of increasing trench widths in the presence of a dynamic thermal field as measured by its effect on long-range order developed and enabling a mechanistic understanding of the synergistic effects of this dual-field DSA method on BCP self-assembly. To our knowledge, these are novel experiments that lead to a new and comprehensive understanding of the geometrical parameters affecting this dual-field approach.

Figure 1a shows the schematic of the CZA instrumental setup. The horizontal temperature gradient is created by an actively controlled hot stage with a cold block on each side. Figure 1b shows optical micrographs of the silicon graphoepitaxy substrates prepared using conventional photolithography and plasma etching that were used for the CZA experiments. The graphoepitaxy substrates have line patterns or channels with constant trench depth of 40 nm and variable trench widths from as narrow as 200 nm to as wide as 2 μm. The long-wave line edge roughness (LER) of the graphoepitaxial patterns is ca. 10 nm. The experiments were therefore performed in a combinatorial manner that ensured that processing conditions were identical for all experiments. The CZA direction was always the same as the graphoepitaxy pattern direction for all experiments reported here. BCP thin film samples are CZA annealed at the rate of 1 μm/s that is statistically equivalent to ≈4 h of oven annealing at 165 °C. The concept of statistical annealing time is reported in detail in the Supporting Information S1. Topography of these films was imaged using an Asylum MFP3D atomic force microscope (AFM) in tapping mode.

Figure 2 shows the typical AFM phase images of the CZA-annealed films on graphoepitaxy substrates in which repeating trenches, "T", are separated by the mesas, "M". The BCP nanostructures within the trench are oriented along the channel direction, whereas BCP nanostructures on top of the mesas are oriented perpendicular to the channel direction. These results are in accordance with the classical observations of epitaxial crystallization where it is found that epitaxial growth is nucleated at the edges of the mesas.[23,39] More importantly, Figure 2 indicates that CZA coupled with graphoepitaxy causes preferential parallel alignment of BCP thin films along the graphoepitaxial pattern direction only within the trenches, and the synergy between graphoepitaxy and CZA needs to be tuned for global alignment of BCP nanostructures. We next discuss the two regimes of CZA-induced graphoepitaxy ordering, (i) symmetric and (ii) asymmetric with respect to T versus M.

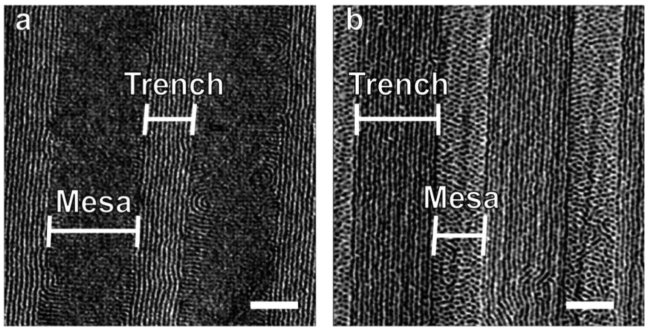

Figure 2. Influence of graphoepitaxy channel geometry on BCP morphology. AFM phase image of the asymmetric PS-PMMA zone annealed at 1 μm/s. The cylinders within the trench are oriented parallel to the channel as expected with few defects. The cylinders on the mesas are oriented perpendicular to the channel. Resolution of the cylinders on the mesas is poor as a result of the AFM scan direction. Size of scale bar is 200 nm.

First we discuss the (i) symmetric pattern (T = M). Here we study the effect of trench width on the BCP long-range order. Since the CZA process does not directly induce alignment on the portion of the BCP thin film on top of the mesas, as seen in Figure 2, only the BCP thin film sections within the trenches are considered in quantifying the orientational order at the surface of these samples. The local thickness of the BCP film remains fairly constant on the mesas and the trenches for symmetric patterns, i.e., ca. 65 nm and ca. 80 nm, respectively. Figure 3 shows the typical false-color cylinder orientation maps observed for samples that were thermally annealed in a vacuum oven at 195 °C for 72 h (Figure 3A,B) and CZA annealed at the rate of 1 μm/s at 210 °C (Figure 3C,D). The procedure to obtain false color maps was explained in detail in our previous publication.[9] Also, the reason for comparing CZA at 1 μm/s and 210 °C with static thermal oven annealing at 195 °C for 72 h is explained in detail in the Supporting Information, S1. The

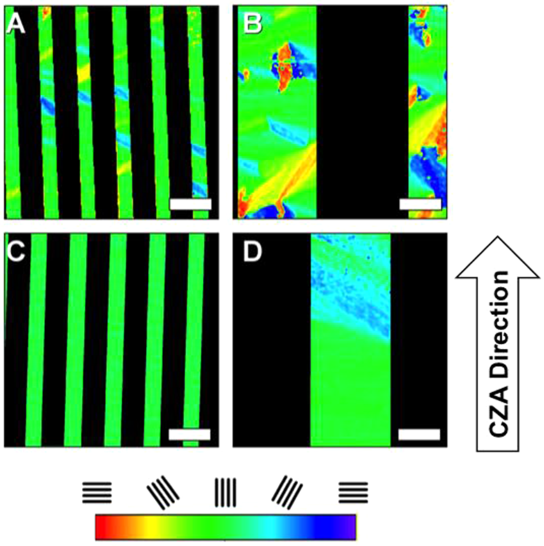

Figure 3. False color image analysis of CZA-annealed thin films on graphoepitaxy channels. (A) and (B) Director angle images for 400 and 2000 nm features, respectively, annealed for 72 h in a vacuum oven at 195 °C. (C) and (D) Director angle images for 400 and 2000 nm features, respectively, cold zone-annealed at 1 μm/s. The mesas have been masked to allow analysis to be performed on only those cylinders within the channel. Size of scale bar is 1 μm.

BCP grain orientation with respect to CZA direction can be directly visualized from the orientation maps; green indicates BCP orientation along the CZA direction, and violet/red indicates BCP orientation orthogonal to the CZA direction. The trench width of graphoepitaxy channels in Figure 3A and Figure 3C is 400 nm and in Figure 3B and Figure 3D is 2000 nm. The presence of multiple colors in Figure 3A,B proves that thermal annealing in a vacuum oven leads to polycrystalline domains even when the BCP thin film is coated on a graphoepitaxy substrate. As expected, the degree of polycrystallinity increases or orientational order decreases as trench width increases.

While qualitatively similar trends are seen for CZA-annealed BCP thin films as well, the CZA annealing fares far better than oven annealing: (i) Figure 3c shows a single crystal of BCP domains oriented in CZA/channel direction, whereas the corresponding oven annealing (Figure 3a) shows a large number of randomly oriented crystals; (ii) Figure 3d shows a mostly distinct green color with a blue phase indicating two distinct but large crystals of BCP domains, whereas the corresponding oven annealing (Figure 3b) again shows multiple crystals which are randomly oriented; and (iii) the time required for oven annealing these films was ≈20× more than the time required for CZA annealing.

Similar analysis, as shown in Figure 3, was performed for the CZA-annealed BCP thin films on graphoepitaxy substrates with variable symmetric trench widths (false color images not shown). The BCP thin film orientational order parameter was calculated from these images using Herman's orientation function "f" (=1 for cylinders aligned parallel, −0.5 for cylinders aligned perpendicular, and 0 for cylinders aligned randomly to CZA/pattern direction, see Figure 4A). Figure 4B is a plot of the calculated Herman's orientation function for the BCP thin films that were CZA annealed and oven annealed on graphoepitaxy substrates with varying trench widths. Herman's orientation function approaches unity as the trench width decreases to 400 nm for CZA-annealed samples and drops to $f \approx 0.6$ as the trench width increases to 2000 nm. In contrast, for oven-annealed samples, $f \approx 0.56$ for a trench width of 400 nm, reducing to $f \approx 0.19$ as the trench width increased to 2000 nm. Excitingly, the lowest f achieved via CZA annealing of the BCP thin films in a fraction of the time was comparable to the maximum achieved $f \approx 0.56$ for 72 h static vacuum oven annealing. The decay of Herman's orientation order with increasing pattern width follows a power law for both CZA and oven annealing with an exponent, $f \sim d^{-0.3}$ for CZA unlike $f \sim d^{-0.7}$ for oven annealing. These observations provide substantial evidence that a dynamic thermal field coupled with a static graphoepitaxy field leads to a considerable improvement in long-range order, unidirectional orientation control, and rapid ordering kinetics as compared to conventional static thermal annealing coupled to the static graphoepitaxy field. Interest-

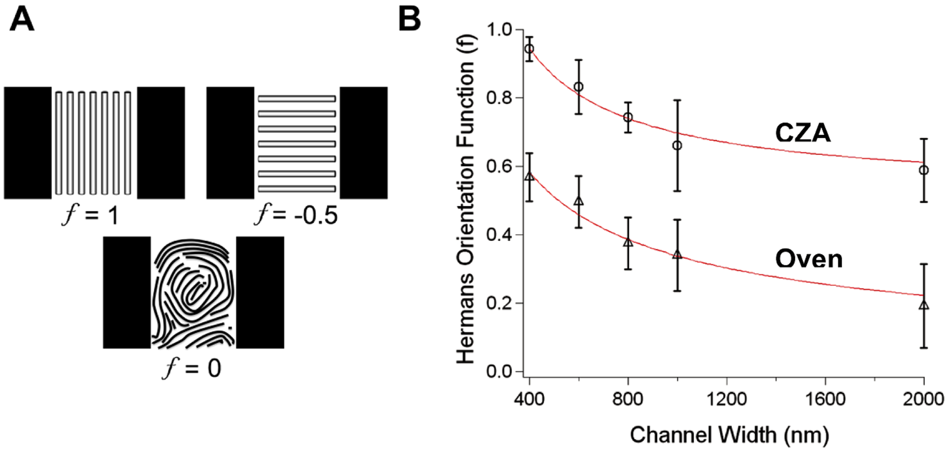

Figure 4. Herman's orientation function analysis of CZA-annealed films on graphoepitaxy channels. (A) Using Herman's orientation function, cylinders perfectly aligned with the channel will produce a value of 1, while cylinders perfectly oriented perpendicular to the channels will result in a value of −0.5. Completely random orientation will produce a value of 0. (B) Plots of Herman's orientation function (f) as a function of channel width for CZA at 1 μm/s (○) and 72 h vacuum oven annealing (△). The combination of CZA with topographical templates produces a significant increase in orientational order compared to traditional oven annealing. The lines are best fits using a power law. The resulting powers for the CZA processed samples and the oven-annealed samples are −0.3 and −0.7, respectively.

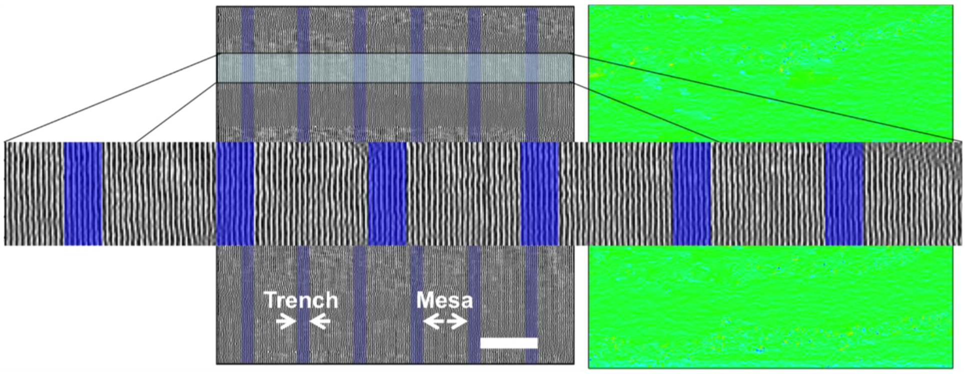

Figure 5. Tuning the synergy of dynamic thermal field and static graphoepitaxy field. AFM phase image of asymmetric PS-PMMA thin film on a graphoepitaxy substrate zone annealed at 1 μm/s and corresponding false-color cylinder-orientation map. Trench width and mesa width of the graphoepitaxy channels are 200 and 600 nm, respectively. Size of scale bar is 800 nm.

ingly, prior work[40−42] on a similar dual-field approach for other systems such as zone melting recrystallization of semiconducting metallic films, for example, silicon and germanium on graphoepitaxy surfaces, and thermal annealing of liquid crystals on graphoepitaxy surfaces exhibited an analogous dependence of the driving force for orientation "f'" on the graphoepitaxy trench width as $f' \sim d^{-1}$.

Next, we discuss the (ii) asymmetric pattern ($T \neq M$). Many nanotechnology applications such as patterned media, plasmonic wave-guides, or nanowire arrays require precise global arrangement of nanostructures, and not just locally such as seen here inside the trenches of the graphoepitaxy channels. In Figure 5, we demonstrate that the synergy between the dynamic thermal field and static graphoepitaxy field can be progressively enhanced to fabricate single-grain unidirectionally aligned horizontal cylinders over the entire sample space (25 μm^2) and not just within the graphoepitaxy trenches as seen in Figure 2.

Although the exact mechanism of the BCP ordering on the asymmetric graphoepitaxy patterns is not known at present, we analyze and correlate the results based on the geometry of the graphoepitaxy patterns. Interestingly, Figure 2 reveals that the cylinders can stretch and compress depending on the confinement width of the trench and the mesa, in accordance with previous results,[43] such that the same film can have two distinct lattice constants. Therefore, we also correlate these results to the local film thickness and local lattice constants. In Figure 2a, Herman's orientation parameter $f = -0.4$ exclusively on the mesas where the asymmetry ratio (ASR) = M/T = 2, whereas in Figure 2b, we observe mixed alignment where ASR = 0.7. The orientation of horizontal cylinders orthogonal to the graphoepitaxy direction has been observed before[43−45] and is attributed to the capillary flow induced alignment of the BCP material from the mesa to the trench. Moreover, the amount of capillary flow of the BCP material into the trenches depends on the trench width and the mesa width. Therefore, depending on the trench width/mesa width, the final local thickness of the BCP film will be different on the trench and the mesa which would then affect the commensurability conditions. It should be noted however that although the ASR ratio indirectly takes into account the effect of trench width and mesa width on the film thickness a more direct comparison of local film thickness to the BCP morphology is equally important. For Figure 2a, we observed that the film thickness on the mesa, trench (M,T) = (65 nm, 80 nm), whereas for Figure 2b, the film thickness on (M,T) = (45 nm, 75 nm). Also, for Figure 2a, the lattice constant over (M,T) = (17 nm, 20 nm), whereas for Figure 2b, the lattice constant over (M,T) = (20 nm, 25 nm). More importantly, the trench width and mesa width can be adjusted to achieve global alignment as shown in Figure 5. The trench width and mesa width that lead to global alignment (i.e., $f \approx 1$) with CZA/line pattern direction in Figure 5 are 200 and 600 nm, respectively, quantified by ASR = 600/200 = 3, i.e., mesa width much bigger than trench width. The critical observation is that if the trench width is made to be very narrow, i.e., ≈200 nm, it not only influences BCP DSA within the trenches but also stimulates BCP alignment over the mesas that leads to global alignment of the BCP thin film. Previously[43] it was observed that prolonged thermal annealing of BCP thin films eventually leads to nucleation of grains oriented along the graphoepitaxial pattern direction on the mesas as well; i.e., prolonged uniform static thermal annealing also leads to global alignment. Here we observe that by a judicious choice of graphoepitaxy pattern dimensions global alignment can be obtained in a small fraction of the annealing time, at the least at an order of magnitude lower. These observations lead us to the conclusion that although trench width is the primary alignment parameter for this dual-field process ASR ratio plays an important role in enhancing the synergy of this dual-field process for the purpose of global BCP alignment. For Figure 5, local film thickness over (M,T) = (65 nm, 84 nm), whereas the lattice constant over (M,T) = (30 nm, 29 nm). Although further studies are indeed required to map out the entire ASR window as well as the local film thickness and lattice constants with changing ASR that lead to global alignment, we strongly believe that this strategy serves as a basis for designing future graphoepitaxy surfaces where the trenches would need to be narrow and are separated by mesas whose width can be several times that of the trench width. Such a strategy would also save the material, time, and energy required to fabricate the graphoepitaxy surfaces, thus reducing the overall cost of BCP DSA.

■ EXPERIMENTAL SECTION

Thin film samples of poly(styrene-block-methylmethacrylate) (PS-PMMA) diblock copolymer were used in these studies. PS-PMMA, total molar mass of 47.5 kg/mol (35 kg/mol − 12.5 kg/mol, PDI ~ 1.07), was bought from Polymer Source Inc. and used as obtained. BCP thin films were coated on ultraviolet−ozone cleaned silicon substrates with graphoepitaxy channels. The thickness of these thin films was ≈71 nm as measured on a flat silicon substrate. The lattice constant for this system in the bulk is ca. 26 nm. Graphoepitaxy substrates were prepared by photolithography and plasma etching, and the depth of these channels was kept fixed at 40 nm. The long-wave line edge roughness (LER) of these patterns was of the order of 10 nm. Prior to the annealing process, the BCP samples were dried at 60 °C for 24 h under vacuum. The procedure for CZA experiments is explained in detail in our recent papers.[9,46] The dynamic thermal gradient approach is based on the original hot-wire design concept by Lovinger et al.[24,38] for directional crystallization of semicrystalline polymers. The maximum temperature (T_{MAX}) of the temperature gradient during zone annealing is 210 °C, and the maximum temperature gradient (∇T) thus developed is 15 C/mm.

■ ASSOCIATED CONTENT

Ⓢ Supporting Information

Explanation on the statistically equivalent annealing time for CZA and static oven annealing. This material is available free of charge via the Internet at http://pubs.acs.org.

■ AUTHOR INFORMATION

Corresponding Author

*Brian C. Berry: (501) 683-7125; bcberry@ualr.edu. Alamgir Karim: (330) 972-8324; alamgir@uakron.edu.

Notes

The authors declare no competing financial interest.

■ ACKNOWLEDGMENTS

We acknowledge NIST Polymers Division (now part of MML), where the experimental aspects of this work were performed while both BB and AK were employed at that time. The analysis aspects of this CZA research work were supported by a collaborative grant between BB and AK and graduate student GS from the National Science Foundation (NSF), Division of Materials Research (DMR), Grant NSF DMR-1006421.

■ REFERENCES

(1) Fasolka, M. J.; Mayes, A. M. *Annu. Rev. Mater. Res.* **2001**, *31*, 323−355.
(2) Bates, F. S.; Fredrickson, G. H. *Annu. Rev. Phys. Chem.* **1990**, *41*, 527−557.
(3) Hamley, I. W. *Prog. Polym. Sci.* **2009**, *34*, 1161−1210.
(4) Darling, S. *Prog. Polym. Sci.* **2007**, *32*, 1152−1204.
(5) Marencic, A. P.; Register, R. A. *Annu. Rev. Chem. Biomol. Eng.* **2010**, *1*, 277−297.
(6) Segalman, R. A. *Mater. Sci. Eng., R* **2005**, *48*, 191−226.
(7) Thurn-Albrecht, T. *Science* **2000**, *290*, 2126−2129.
(8) Bodycomb, J.; Funaki, Y.; Kimishima, K.; Hashimoto, T. *Macromolecules* **1999**, *32*, 2075−2077.
(9) Berry, B. C.; Bosse, A. W.; Douglas, J. F.; Jones, R. L.; Karim, A. *Nano Lett.* **2007**, *7*, 2789−2794.
(10) Singh, G.; Yager, K. G.; Smilgies, D.-M.; Kulkarni, M. M.; Bucknall, D. G.; Karim, A. *Macromolecules* **2012**, *45*, 7107−7117.
(11) Singh, G.; Yager, K. G.; Berry, B.; Kim, H.-C.; Karim, A. *ACS Nano* **2012**, *6*, 10335−10342.
(12) Angelescu, D. E.; Waller, J. H.; Adamson, D. H.; Register, R. A.; Chaikin, P. M. *Adv. Mater.* **2007**, *19*, 2687−2690.
(13) Angelescu, D. E.; Waller, J. H.; Adamson, D. H.; Deshpande, P.; Chou, S. Y.; Register, R. A.; Chaikin, P. M. *Adv. Mater.* **2004**, *16*, 1736−1740.
(14) Wu, M.; Register, R. A.; Chaikin, P. *Phys. Rev. E* **2006**, *74*, 1−4.
(15) Marencic, A.; Chaikin, P.; Register, R. A. *Phys. Rev. E* **2012**, *86*, 1−8.
(16) Hong, S. W.; Huh, J.; Gu, X.; Lee, D. H.; Jo, W. H.; Park, S.; Xu, T.; Russell, T. P. *Proc. Natl. Acad. Sci. U.S.A.* **2012**, *109*, 1402−1406.
(17) Hong, S. W.; Voronov, D. L.; Lee, D. H.; Hexemer, A.; Padmore, H. A; Xu, T.; Russell, T. P. *Adv. Mater.* **2012**, *24*, 4278−4283.
(18) Sivaniah, E.; Hayashi, Y.; Matsubara, S.; Kiyono, S.; Hashimoto, T.; Fukunaga, K.; Kramer, E. J.; Mates, T. *Macromolecules* **2005**, *38*, 1837−1849.
(19) Kulkarni, M. M.; Yager, K. G.; Sharma, A.; Karim, A. *Macromolecules* **2012**, *45*, 4303−4314.
(20) Tang, C.; Tracz, A.; Kruk, M.; Zhang, R.; Smilgies, D.-M.; Matyjaszewski, K.; Kowalewski, T. *J. Am. Chem. Soc.* **2005**, *127*, 6918−6919.
(21) Kim, S. H.; Misner, M. J.; Xu, T.; Kimura, M.; Russell, T. P. *Adv. Mater.* **2004**, *16*, 226−231.
(22) Tang, C.; Lennon, E. M.; Fredrickson, G. H.; Kramer, E. J.; Hawker, C. J. *Science* **2008**, *322*, 429−432.
(23) Segalman, R. A.; Yokoyama, H.; Kramer, E. J. *Adv. Mater.* **2001**, *13*, 1152−1155.
(24) Park, S.; Rettner, C. T.; Pitera, J. W.; Kim, H. *Macromolecules* **2009**, *42*, 5895−5899.
(25) Cheng, J. Y.; Mayes, A. M.; Ross, C. A. *Nat. Mater.* **2004**, *3*, 823−828.
(26) Kim, S. O.; Solak, H. H.; Stoykovich, M. P.; Ferrier, N. J.; De Pablo, J. J.; Nealey, P. F. *Nature* **2003**, *424*, 411−414.
(27) Ruiz, R.; Kang, H.; Detcheverry, F. A.; Dobisz, E.; Kercher, D. S.; Albrecht, T. R.; De Pablo, J. J.; Nealey, P. F. *Science* **2008**, *321*, 936−939.
(28) Edwards, E. W.; Montague, M. F.; Solak, H. H.; Hawker, C. J.; Nealey, P. F. *Adv. Mater.* **2004**, *16*, 1315−1319.
(29) Han, E.; Stuen, K. O.; Leolukman, M.; Liu, C.-C.; Nealey, P. F.; Gopalan, P. *Macromolecules* **2009**, *42*, 4896−4901.
(30) Kim, S.; Shin, D. O.; Choi, D.-G.; Jeong, J.-R.; Mun, J. H.; Yang, Y.-B.; Kim, J. U.; Kim, S. O.; Jeong, J.-H. *Small* **2012**, *8*, 1563−9.
(31) Resnick, D. J.; Sreenivasan, S. V; Willson, C. G. *Mater. Today* **2005**, *8*, 34−42.
(32) Chou, S.; Krauss, P. R.; Renstrom, P. J. *J. Vac. Sci. Technol. B* **1996**, *14*, 4129−4133.
(33) Zhang, X.; Harris, K. D.; Wu, N. L. Y.; Murphy, J. N.; Buriak, J. M. *ACS Nano* **2010**, *4*, 7021−7029.
(34) Bates, C. M.; Seshimo, T.; Maher, M. J.; Durand, W. J.; Cushen, J. D.; Dean, L. M.; Blachut, G.; Ellison, C. J.; Willson, C. G. *Science* **2012**, *338*, 775−779.
(35) Mishra, V.; Fredrickson, G. H.; Kramer, E. J. *ACS Nano* **2012**, *6*, 2629−2641.
(36) Park, S.-M.; Stoykovich, M. P.; Ruiz, R.; Zhang, Y.; Black, C. T.; Nealey, P. F. *Adv. Mater.* **2007**, *19*, 607−611.
(37) Park, W. I.; Kim, K.; Jang, H.-I.; Jeong, J. W.; Kim, J. M.; Choi, J.; Park, J. H.; Jung, Y. S. *Small* **2012**, *8*, 3762−3768.
(38) Pfann, W. G. *Science* **1962**, *135*, 1101−1109.
(39) Kim, H.-C.; Park, S.-M.; Hinsberg, W. D. *Chem. Rev.* **2010**, *110*, 146−223.
(40) Smith, H. I.; Geis, M. W.; Thompson, C. V.; Atwater, H. A. *J. Cryst. Growth* **1983**, *63*, 527−546.
(41) Sakano, K.; Moriwaki, K.; Aritome, H.; Namba, S. *Jpn. J. Appl. Phys.* **1982**, *21*, L636−L638.
(42) Flanders, D. C.; Shaver, D. C.; Smith, H. I. *Appl. Phys. Lett.* **1978**, *32*, 597−598.
(43) Sundrani, D.; Darling, S. B.; Sibener, S. J. *Nano Lett.* **2004**, *4*, 273−276.
(44) Sundrani, D.; Darling, S. B.; Sibener, S. J. *Langmuir* **2004**, *20*, 5091−5099.
(45) Fitzgerald, T. G.; Farrell, R. A.; Petkov, N.; Bolger, C. T.; Shaw, M. T.; Charpin, J. P. F.; Gleeson, J. P.; Holmes, J. D.; Morris, M. A. *Langmuir* **2009**, *25*, 13551−13560.
(46) Yager, K. G.; Fredin, N. J.; Zhang, X.; Berry, B. C.; Karim, A.; Jones, R. L. *Soft Matter* **2010**, *6*, 92−99.